Wind tunnel and computational fluid dynamics study of wind conditions in an urban square

Márton Balczó[*] and **András Tomor**

Theodore von Kármán Wind Tunnel Laboratory
Department of Fluid Mechanics, Faculty of Mechanical Engineering,
Budapest University of Technology and Economics
Bertalan L. u. 4-6, H-1111 Budapest, Hungary

Authors E-mail: balczo@ara.bme.hu; tomor@ara.bme.hu

[*]*Corresponding author*

Abstract—Recognizing the role of urban squares in city life, the paper focuses on wind conditions at squares, with the objective to understand the building-scale flow phenomena influencing the wind comfort of pedestrians and the dispersion of pollutants. Wind tunnel testing of a selected square has been carried out at two wind directions, as well as accompanying computational fluid dynamics (CFD) simulations were performed using the MISKAM microscale model. The high spatial resolution experimental and CFD data allowed the identification of flow structures, like separation bubbles, vortices, high-speed zones in and around the square. Based on the analysis of numerical and experimental data obtained, the MISKAM model is able to resolve the flow field in a complex urban setting with some limitations. In a second step, the model was then used to run further numerical simulations, to compare fully built-up areas to an area with a square, and to assess the influence of tree plantings on the square. Results regarding the latter indicate that below tree crown height, flow velocity and turbulent kinetic energy are both decreased by about one fourth due to the vegetation. It is also shown that the presence of the square increases wind speed in connecting streets and induces longitudinal flows even in streets perpendicular to the approaching wind direction. The time-resolved wind tunnel measurements also allowed presenting the local velocity statistics as wind roses. Using these, we identified locations with non-isotropic turbulence and alternating wind directions.

Key-words: urban square, flow field, velocity fluctuation, urban vegetation, wind tunnel

1. Introduction

Urban flow and dispersion has been the subject of hundreds of research papers in the past, though only review articles (*Britter* and *Hanna,* 2003; *Ahmad et al.,* 2005; *Belcher et al.,* 2013; *Blocken,* 2014) may be cited here. While there is a huge selection of studies on ventilation and pollutant dispersion in urban street canyons, street intersections and regular arrangements of building blocks, there are few detailed analyses of the flow and dispersion phenomena specifically at urban squares. A square is defined as an open, typically four-sided area surrounded by buildings, with length to width ratio not necessarily equaling one. Squares fulfil important functions in urban life: they facilitate playing and sporting grounds, dining opportunities, markets, and open-air events. The creation of squares from the demolition of defunct residential or industrial buildings is an option in urban redevelopment programs. The longer residence time of pedestrians on squares explains why wind conditions and pollutant dispersion are of interest.

Only a few papers dealt with air pollution and flow phenomena specifically in urban squares. *Gadilhe et al.,*(1993) studied a semi-circular square and found recirculation zones behind the upstream located buildings of the square. *Parra et al.* (2010) showed using CFD simulations that depending on wind direction, locally released pollutants can be trapped in the separation vortices behind those buildings, and concentration distribution on the square is quite inhomogeneous. Obstacle resolving test cases of whole districts like the 'Michel-Stadt' semi-idealized urban dataset of *Bastigkeit* (2011) also include squares, among other features of an urban geometry, so there is experimental and numerical data available (*Hertwig et al.,* 2012; *Rákai* and *Kristóf,* 2013). However, the specialities of the flow in the squares were not separately addressed in these studies. Also, measurement data with higher spatial resolution would allow a more detailed analysis of the flow in the squares.

In the present paper, a typical urban square, József Nádor Square (coordinates 47.498 N, 19.050 E) in downtown Budapest will be investigated. It measures approximately 150×60 m, and is surrounded from all sides by building blocks of 28 m average height. The connecting streets are relatively narrow; their width to height (*w/h*) ratio is about 0.5. The square has unfavorable ventilation. Moreover, on its northern side it is bordered by the extremely busy József Attila Street with approx. 2000 vehicles/hour in rush hours, emitting a considerable amount of pollutants.

The area is heavily polluted with concentration levels well above the limit, as it was proven in an earlier paper (*Balczó* and *Lajos,* 2012), in which we investigated the site by using CFD simulations of the surroundings. The annual averages of NO_x concentrations at ground level in the north of the square showed values about twice as high as the annual limit. Also, the data of the on-site air quality monitoring station was analyzed and compared to the CFD

results. CFD predictions of annual NO_x averages deviated just 16% or less from the measured concentration values.

In the present study, wind tunnel measurements of a 1:350 scale model and computational fluid dynamics (CFD) simulations were carried out to understand the flow phenomena in the square and its surroundings. The flow field measurements were performed in a Göttingen-type wind tunnel by using laser-doppler velocimetry (LDV). In order to achieve proper flow field results, an urban-type atmospheric boundary layer was modeled in the wind tunnel and checked by vertical profile measurements.

The flow around exactly the same model geometry was simulated using the MISKAM flow and dispersion model, developed by *Eichhorn et al.*(1988). This CFD model solves the Reynolds-averaged Navier-Stokes (RANS) equations on a Cartesian non-equidistant grid and applies a modified K-ε closure adapted to urban flows. In the next step, the dispersion of pollutants can be calculated by solving the Reynolds-averaged advective diffusion equation. For detailed description of the current version 6, see *Eichhorn* (2011). The model underwent detailed evaluation in the past decade both according to the evaluation guideline VDI 3783/9 (*VDI,* 2005) performed by *Eichhorn* and *Kniffka* (2010) and it also took part in the model evaluation study of the European research Action COST 732 (*Schatzmann et al.,* 2010). Evaluation using the more complex MUST data set was published by *Balczó* and *Eichhorn* (2009) and *Goricsán et al.* (2011), testing with other data sets by *Olesen et al.* (2009).

The MISKAM model is able to run on standard personal computers, and its applicability to problems in urban environment has been shown in several publications (*Benson et al.,* 2007; *Balczó et al.,* 2009; *Donnelly et al.,* 2009; *Belalcazar et al.,* 2010; *Flassak et al.,* 2010; *Balczó et al.,* 2011). MISKAM was used as wind field and turbulence input for other dispersion models (*Leuzzi et al.,* 2010; *Letzel et al.,* 2012).

Due its simple setup and handling, the code is not only used by experts with deep knowledge of fluid dynamics, but also by many environmental agencies, authorities, and consulting engineers. While the application of high-end CFD models (e.g., LES) is not realistic in the regulatory / air quality assessment field at the present, MISKAM and other purpose-built RANS models form a significant step forward from earlier non-CFD (Gaussian, empirical, etc.) models applied in this area, when more accuracy in urban micro scale investigations is needed. Thus, the secondary objective of this work is to assess the capabilities of a CFD RANS model intended for regulatory use on complex real-world geometry.

2. Experimental setup

2.1. Wind tunnel and measurement setup

Experiments were carried out in the 3.8 m long and 2.6 m wide open test section of the large horizontal wind tunnel of the Budapest University of Technology and Economics. Model and boundary layer generation devices are mounted on a horizontal plate of 2.5 m width. *Fig. 1* shows the measurement layout. During the measurements, the fibre-optic laser doppler velocimetry (LDV) probe accessed the flow from below through a glass plate; therefore, the flow was not disturbed by the probe. A two-component LDV system was applied; hence, the horizontal velocity components u and v could be determined using the mentioned arrangement. The system consists of an air-cooled 300 mW Argon-Ion laser, generating a multiple frequency beam which goes through beam splitter and a Bragg cell to generate shifted and unshifted 488 and 514.5 nm (blue and green) beams. The four beams then pass through a fibre optic cable towards the LDV optics with 363 mm focal length and 61 mm clear aperture. Measurement volume has a diameter of 90 μm and 1.3 mm length. Laser light from the olive oil seeding particles passing the measurement volume is reflected back into the optics leading to photomultipliers and then digitized and analyzed by FSA3500 DSP-based signal processing unit. Burst frequencies are determined by autocorrelation. Burst velocities are weighted with gate time to get average velocities.
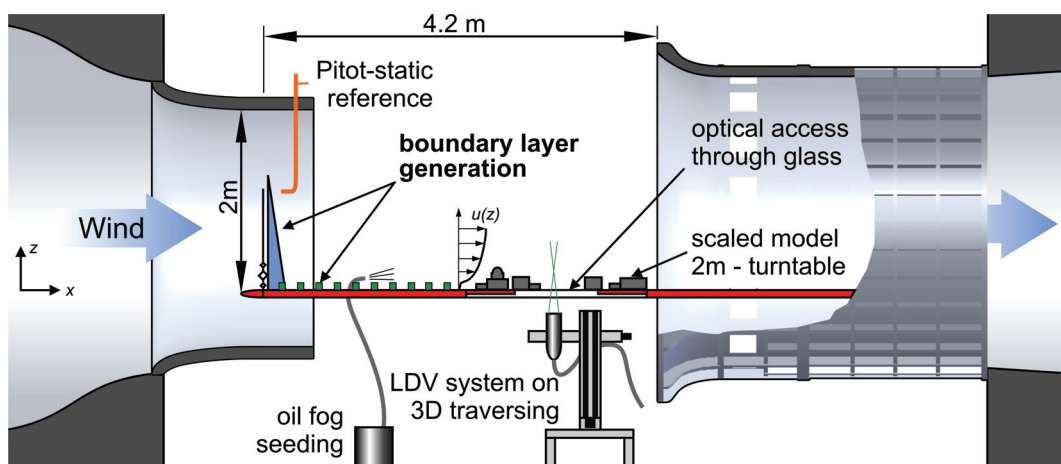

Fig. 1. The measurement layout including spikes, crossbars, and roughness elements in the preparatory section of the wind tunnel, the model arranged in the test section of the wind tunnel, and the LDV probe below the test section.

During the test campaign, different averaging times were used. At the incoming boundary layer measurement (Subsection 2.2), 200.000 velocity samples (bursts) were collected in up to 5 min, and during the flow field measurement of the square (Subsection 2.3), about 5000 samples were collected during the selected 50 s averaging time. The representativeness of measured velocity averages and standard deviations was checked during a few measurements of longer duration.

2.2. Atmospheric boundary layer generation

Following the well-established procedure of boundary layer generation in wind tunnels (see, e.g., *Gromke* and *Ruck,* 2005) and *Kozmar* (2011), an urban-type atmospheric boundary layer was generated in the wind tunnel modeling the natural ABL described in ESDU 72026 (*ESDU,* 1972), ESDU 85020 (*ESDU,* 2001), and VDI 3783/12 (*VDI,* 2004) by placing vortex generators, crossbars, and roughness elements into the preparatory section of the wind tunnel. The mentioned arrangement can be seen in *Fig. 1*. Vertical profiles of the developed boundary layer were measured using the LDV system at the centre of the turntable without the city model. Boundary layer parameters were determined from the mean velocities $\bar{u}(z)$ and $\bar{v}(z)$ in streamwise and lateral direction; as well as from their respective standard deviations $\sigma_u(z)$ and $\sigma_v(z)$. Turbulence intensity in the x- and y-direction (I_u and I_v) are defined as $\sigma_u(z)\,/\bar{u}(z)$ and $\sigma_v(z)\,/\bar{v}(z)$. Longitudinal integral length scale of turbulence using autocorrelation is given by:

$$L_{u,x} = \int_0^\infty R_{uu}(\Delta x)d\Delta x, \qquad (1)$$

with R_{uu} – autocorrelation coefficient of the of the $u(z,t)$ – velocity time-series in x-direction.

Fig. 2 shows the profile of the dimensionless mean velocity into the main flow direction (a) and the turbulence intensity profiles I_u and I_v (b and c). Mean velocity $\bar{u}$ was approximated with the power law in the form

$$\frac{\bar{u}(z)}{u_{ref}} = \left(\frac{z - d_0}{z_{ref} - d_0} \right)^\alpha, \qquad (2)$$

where α is the exponent, z is the height, z_{ref} is the reference height (height of the modeled boundary layer), u_{ref} is the mean velocity at the reference height and d_0 is the displacement height. In order to obtain dimensionless mean velocities,

local velocities $\bar{u}(z)$, were divided by the reference velocity $u_{ref} = 4.60$ m/s, which was measured at the reference height $z_{ref} = 309.50$ mm (108 m full scale).
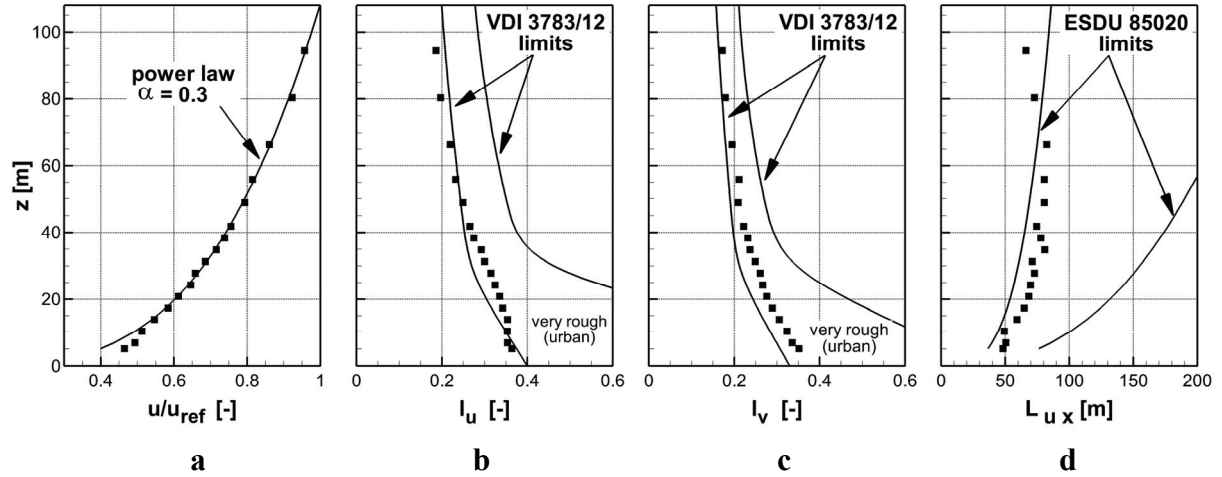

Fig. 2. Approach flow variables as a function of full scale height: (a) dimensionless mean velocity u/u_{ref}; (b) streamwise turbulence intensity I_u compared with urban type ABL turbulence given in VDI 3783/12; (c) lateral turbulence intensity I_v; (d) streamwise integral length scale of turbulence $L_{u,x}$ compared with ESDU 85020 data.

Displacement height was considered to be zero at the boundary layer measurement without the city model. (In measurements with the model on the turntable, the first few rows of buildings will elevate the boundary layer to the displacement height of ~ 0.75 h, as it can be seen later in the profiles of *Figs. 7–9*.)

The above parameters of an urban-type atmospheric boundary layer are specified by several guidelines and standards. According to ESDU (1972), the power law exponent $\alpha = 0.3$ can be accepted for the representation of the urban atmospheric boundary layer. Turbulence intensity I_u profile shows some differences compared with VDI (2004) data; however, below the full scale height of 60 m, the agreement between the standard and measured data is perfect.

The integral length scale profile $L_{u,x}$ is shown in *Fig. 2 (d)*. The $L_{u,x}$ values – scaled up using the scale factor 1:350 – were compared with ESDU (2001) data. The integral length scale profile $L_{u,x}$ agrees well with the suggestions of the standard except above 80 m full scale height.

Based on the profile measurements, the generated atmospheric boundary layer was considered to be an accurate model of the ABL approaching the investigated square.

2.3. Model construction and the final measurement layout

The 1:350 scale model of the quarter around József Nádor Square was modeled with buildings prepared using waterjet-cut plywood and hotwire-cut rigid foam, and the whole model was placed on a wooden circular plate with a diameter of 2 m. An 800 × 800 mm opening in the middle of the plate covered by a pane of glass provided optical access to the flow from beneath the model. Although roof shape has certain effects on the flow, these effects were neglected in order to simplify the CFD model and mesh generation. According to this, the buildings of the experimental model were also modeled as blocks with flat rooftops and classified heights in 1.5 m steps. József Nádor Square and the surrounding quarter can be seen in *Fig. 3*, the model is shown in *Fig. 4*, left.
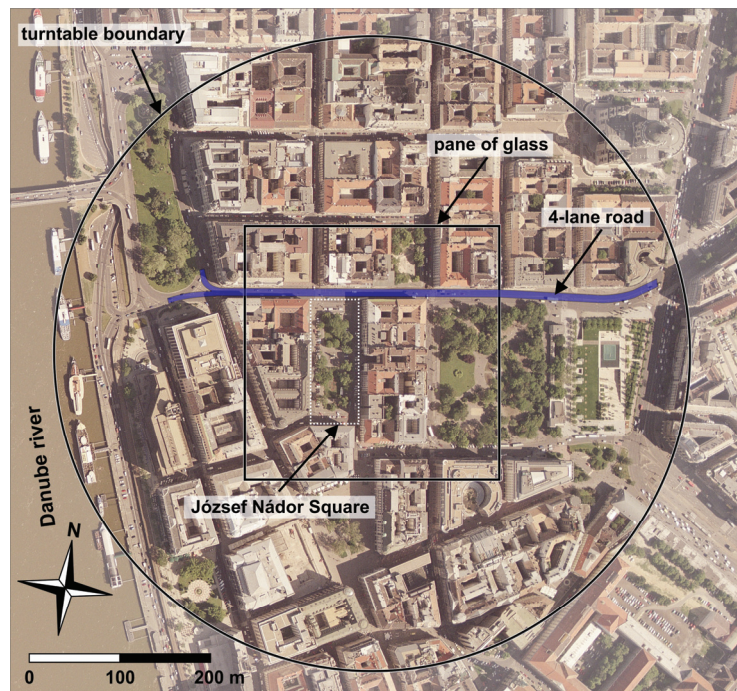

Fig. 3. Aerial photograph of József Nádor Square and the surrounding quarter; the edge of the wooden turntable and the pane of glass are also marked.

Flow velocities were measured along 23 vertical profiles and three horizontal planes (see later in *Fig. 5*). Local mean velocities, $\bar{u}$ and $\bar{v}$, were normalized to the reference velocity u_{ref} = 3.02 m/s, which was measured at the building mean height h = 80 mm during the boundary layer measurements; h is the mean building height in model scale. The mean building height in full scale is h = 28 m.
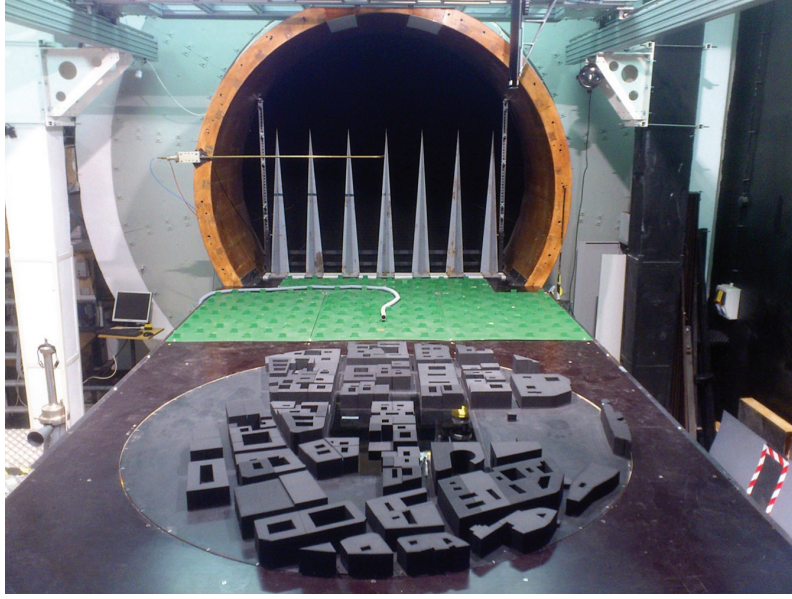
Fig. 4. The model in wind tunnel. Buildings are painted black to reduce laser reflections.

The parameters discussed herein can be calculated with the following formulas. Dimensionless mean velocity u_d and v_d in the *x*- and *y*-direction is calculated as $u_d = \bar{u}/u_{ref}$ and $v_d = \bar{v}/u_{ref}$, respectively. Dimensionless velocity fluctuations σ_{ud} and σ_{vd} are defined as $\sigma_{ud} = \sigma_u/u_{ref}$ and $\sigma_{vd} = \sigma_v/u_{ref}$ with velocity standard deviations σ_u and σ_v.

Dimensionless horizontal mean velocity magnitude v_{md} :

$$v_{md} = \sqrt{u_d^2 + v_d^2}. \tag{3}$$

Dimensionless turbulent kinetic energy K_d :

$$K_d = \frac{1}{2} \cdot \left(\sigma_{ud}^2 + \sigma_{vd}^2 \right). \tag{4}$$

It must be noted that the calculated turbulent kinetic energy calculated from Eq. (4) differs from the real one, because the vertical velocity component *w* and its standard deviation σ_w could not be measured using the applied arrangement. Thus, K_d is the contribution of horizontal velocity components to turbulent kinetic energy.
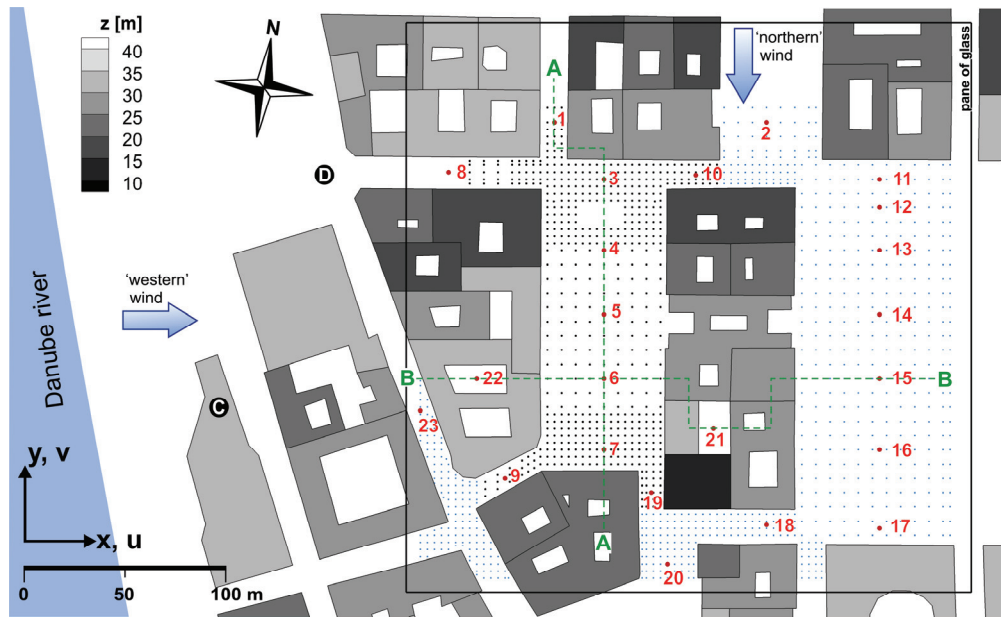
Fig. 5. Wind directions and measurement locations on the wind tunnel model. Buildings are colored by their full scale height. Red circles: vertical profile (VP) measurements; black dots: horizontal plane measurements at 0.25 *h*, 0.5 *h*, and *h* heights; blue dots: additional horizontal plane measurements at 0.5 *h* height.

2.4. *Wind directions*

During the flow field measurements in the model of József Nádor Square, two wind directions were investigated: approximately northern wind direction, 351.7 degree to north, and 261.7 degree to north, approximately western wind direction. The selected two wind directions mean that wind blows at 'northern' wind exactly along the long axis of the square, at which its length to height ratio *l/h* of the square is 5.3, and at 'western wind' exactly along the short axis of the square with *l/h* equaling 2.1. Wind statistics were available from three neighboring meteorological stations, which are in 2.5–10 km distance. Their averaged wind rose shows north and west-northwest as the prevailing wind directions, thus the selected wind directions are close to the prevailing ones.

3. *Numerical setup*

Setup of the CFD simulation carried out at 'northern' (351.7 deg) wind direction followed the best practice guideline given by *Franke et al.* (2007). The computational domain included the buildings modeled in the wind tunnel in full scale inside a 700 m diameter circle around József Nádor Square corresponding to the 2 m diameter turntable, with proper inlet, outlet, and side distances to the domain boundary. Domain size was thus $1000 \times 1100 \times 500$ m. Grid resolution of the non-equidistant Cartesian grid applied by MISKAM varied from 4–6 m

horizontally and 1 m vertically between buildings down to 1.5 m horizontally and 0.6 m vertically around József Nádor Square near the ground, up to a total of approximately 5 million grid cells.

Regarding grid independency of the computational mesh, earlier MISKAM simulations of a simplified symmetrical street canyon geometry by *Balczó et al.* (2009) showed that it can be reached at an average of 0.5 m cell size (with refinements of 0.1 m at building leading edges). However, this resolution could not be replicated in the current complex, large-domain case with hundreds of buildings due to memory limitations of the 32 bit code. The current resolution can be seen as typical for the MISKAM model when applied in environmental impact assessment studies by agencies on a daily basis.

The predefined boundary condition types of MISKAM (see *Eichhorn,* 2011) were used: buildings represented as block outs from the Cartesian grid, on the surfaces no-slip conditions applied using wall functions, the roughness length on the surfaces set to 0.01 m. At the inlet boundaries an equilibrium logarithmic profile was generated by MISKAM automatically with initial roughness length z_0 of 0.2 m. The reference velocity was set to 3.02 m/s at $h=28$ m, as measured in wind tunnel.

The comparison of the CFD approaching flow profile to the profile measured in the empty wind tunnel shows certain disagreement in terms of both mean velocity and turbulence (*Fig. 6*).Turbulence underestimation in boundary layer profiles over flat terrain is a common error of K-ε turbulence closures as shown, e.g., by *Olesen et al.* (2008). It is expected, however, that the first few rows of buildings will act as boundary condition generators, and the profiles will be assimilated to each other. This will be checked later comparing CFD and wind tunnel vertical velocity profiles at locations near the square.
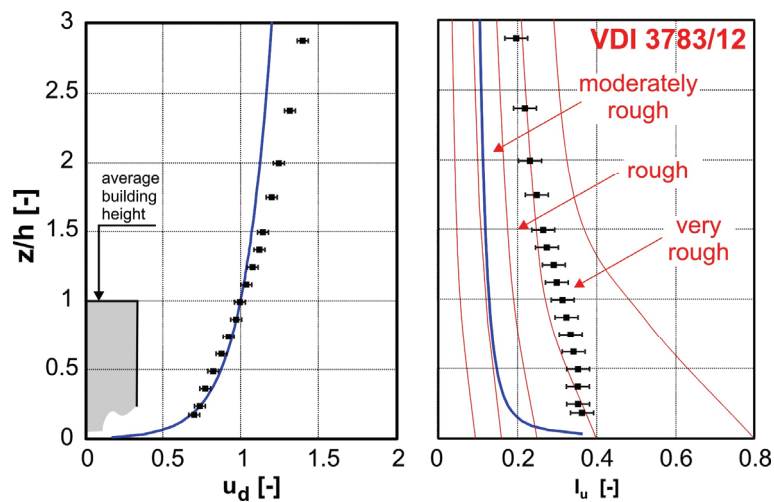

Fig. 6. Streamwise u_d dimensionless velocity and I_u turbulence intensity profiles. Simulation: continuous blue line, wind tunnel measurement: dots with error bars. *h*: average building height. Red lines: VDI 3783/12 limits.

4. Results and discussion

In the course of the analysis of results, first we will identify the major flow structures using vertical profile diagrams, and velocity and turbulence plots in horizontal planes in Sections 4.1 and 4.2. Although the vertical velocity component was not directly measured, some of the data allow us to draw conclusions about the vertical velocities and the three dimensional flow structures in Section 4.3. Section 4.4 shows time-resolved wind tunnel data in order to analyze unsteady phenomena in the square. In Section 4.5, the flow in the square is compared statistically with the flow in neighboring streets and to a case in which the square is replaced by a block of buildings. Additionally, we assess the influence of street vegetation in Section 4.6, and then discuss the performance of the CFD model in Section 4.7.

In the following comparison plots, turbulent kinetic energy K_d determined in simulations was always multiplied by 2/3, in order to approximate the contribution of horizontal velocity fluctuations to the turbulent kinetic energy, which was actually measured in the wind tunnel.

4.1. *Analysis of vertical profiles*

The 23 dimensionless vertical velocity profiles give a first insight into the flow field at the square. Our expectation is that the streamwise velocity component (*v* in case of northern wind direction) will follow the approaching wind profile (*Fig. 6*) above rooftop level, but around and below rooftop level it will deviate significantly.

Fig. 7 shows vertical profiles of mean velocity from both the wind tunnel and CFD simulation, streamlines from CFD and turbulent kinetic energy from the wind tunnel in the mid-plane of the square (cross section A-A in *Fig. 5*). The building located at the northern end of the square generates backflow (marked with A in *Fig. 7*). The presence of this recirculation zone is visible on profiles VP3 and VP4. The streamlines originating from one source point indicate that there is significant inflow from x direction (from the connecting street) into the core of the separation zone.

From the middle of the square (approximately 2.5 *h* distance, B in *Fig. 7*)), streamlines reach the bottom on the square and stagnation point develops in front of the downstream building block. Close to the ground (marked with C in *Fig. 7*), again backflow can be observed in the wind tunnel measurements, showing the presence of a *horseshoe vortex*, which is unfortunately not resolved by the CFD. Otherwise, CFD follows the measurements quite well, especially above rooftop level, proving the assumption made earlier, that the slight differences in incoming boundary conditions are assimilated, as the flow reaches the square. Near the ground, the streamwise flow velocities are overestimated by CFD.
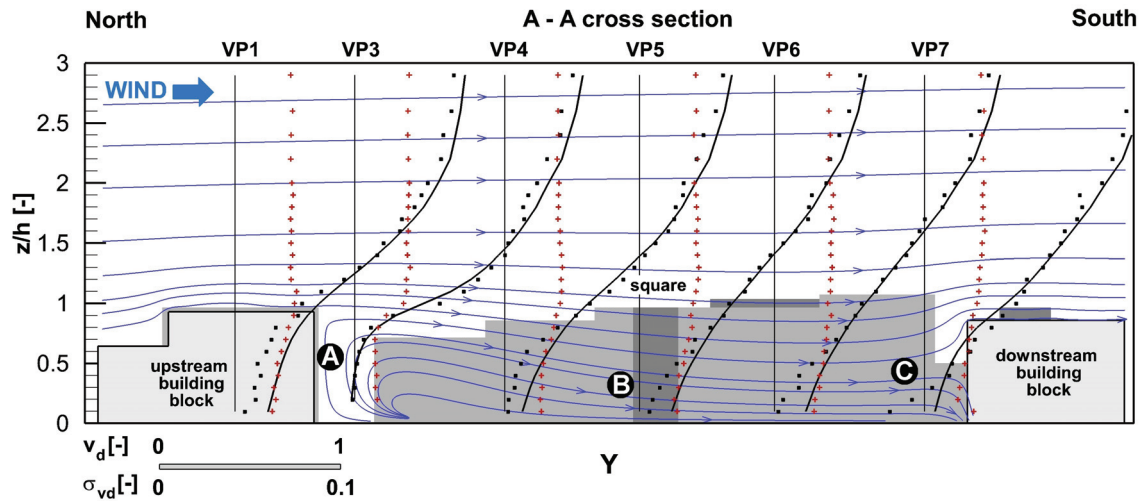
Fig. 7. Flow field at northern wind direction along the square (A –A cross section of *Fig. 5*). Black squares and continuous lines: normalized streamwise mean velocity component v_d from measurement and simulation, crosses: normalized velocity standard deviation σ_{vd} from wind tunnel measurement. Streamlines in blue are from the simulation. Note that VP1 lies in a connecting street, not on the square itself.

The flow field in a cross-section of the square at western wind is depicted in *Fig. 8* (cross section B - B of *Fig. 5*). In this direction, the square is only 2 *h* wide.

- Measurement shows strong backflow on the square up to rooftop level (VP6). Streamlines indicate a vortex with horizontal axis dominating the whole square. Similar backflow can be seen behind the downstream building block.

- Despite their small size, building inner yards have street-canyon-like horizontal vortices (VP22, VP21).

At both wind directions, turbulent kinetic energy K_d is almost constant above rooftop level (with an occasional, slight maximum at 1.2–1.7 h height), and decreases underneath rooftop level towards the ground by about one third. In building inner yards, its value goes down to less than one half.

For the generalized, quantitative description of the flow in urban squares, we compare the averaged vertical velocity profiles in the square (VP 3–7) at the two wind directions in *Fig. 9*. While above 1.5 *h*, all profiles run close together, there are differences below that level. Most remarkably, at western wind, speeds are higher than at northern wind. Nevertheless, in none of the cases it is higher than 0.5. Also, compared to the averaged profiles measured in the connecting streets (VP 1, 8, 9, 10, 18, 23), wind speed in the square is approximately the same.

CFD results, available at northern wind direction, overlap almost perfectly the wind tunnel measurement data.
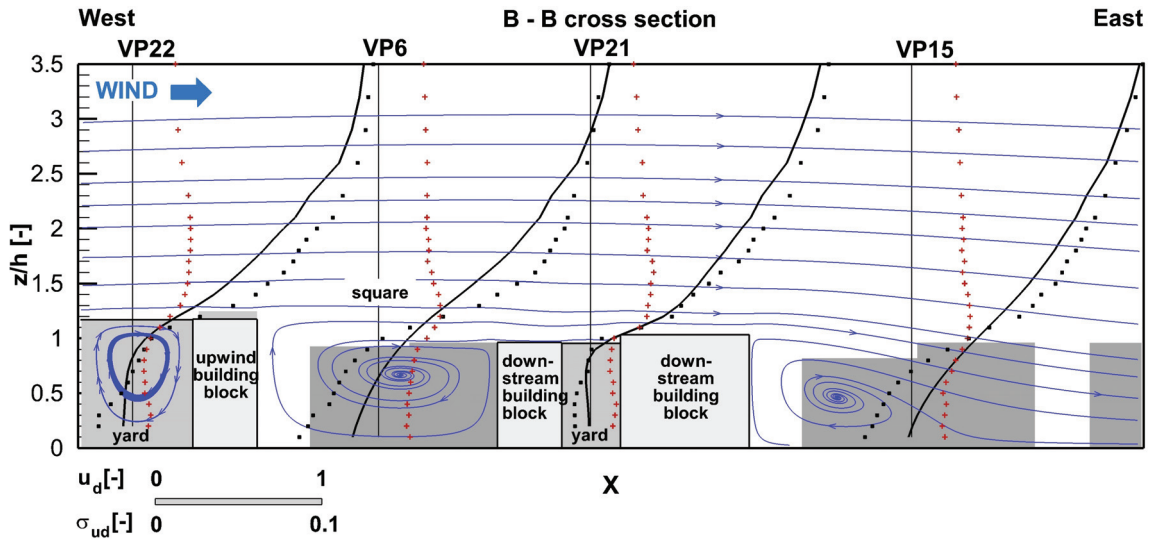
Fig. 8. Flow field at western wind direction along the square (B – B cross section of *Fig. 5*). Black squares: normalized streamwise mean velocity u_d from measurement, crosses: normalized velocity standard deviations σ_u from wind tunnel measurement. Streamlines are from simulation. Please note that profile VP21 is about 30 m off-plane towards south.
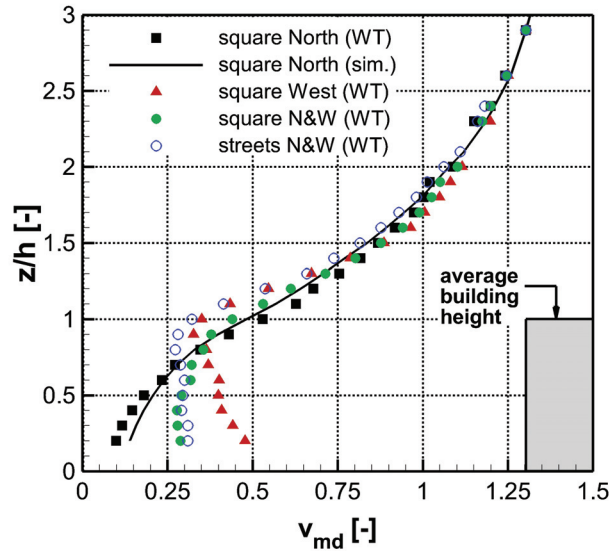

Fig. 9. Averaged vertical profiles of velocity magnitude v_{md} in the square (VP 3-7). Black: at northern, red: at western wind direction. For comparison, an overall average of vertical profiles in the connecting streets (VP 1, 8, 9, 10, 18, 23) is shown with blue.

4.2. Flow field in horizontal planes

Flow velocities were measured along three horizontal planes at 0.25 *h*, 0.5 *h*, and *h*, corresponding to 7, 14, and 28 m in full scale (20, 40, 80 mm in model scale).

Planes 1 and 3 included 568 measurement points; plane 2 consists of 1287 points (see *Fig. 5*). The positioning accuracy was less than 0.5 mm. The normalized horizontal velocity magnitude v_{md} at northern wind direction on the three horizontal planes can be seen in *Fig. 10,* with wind tunnel data in the left and CFD data in the right column. *Fig. 11* shows the normalized turbulent kinetic energy distributions in the same wind direction. *Fig. 12* shows the same variables but in western wind direction. Scalar variables are interpolated from the measurement points onto the planes using inverse-distance interpolation, and streamlines are integrated from the velocity vectors.
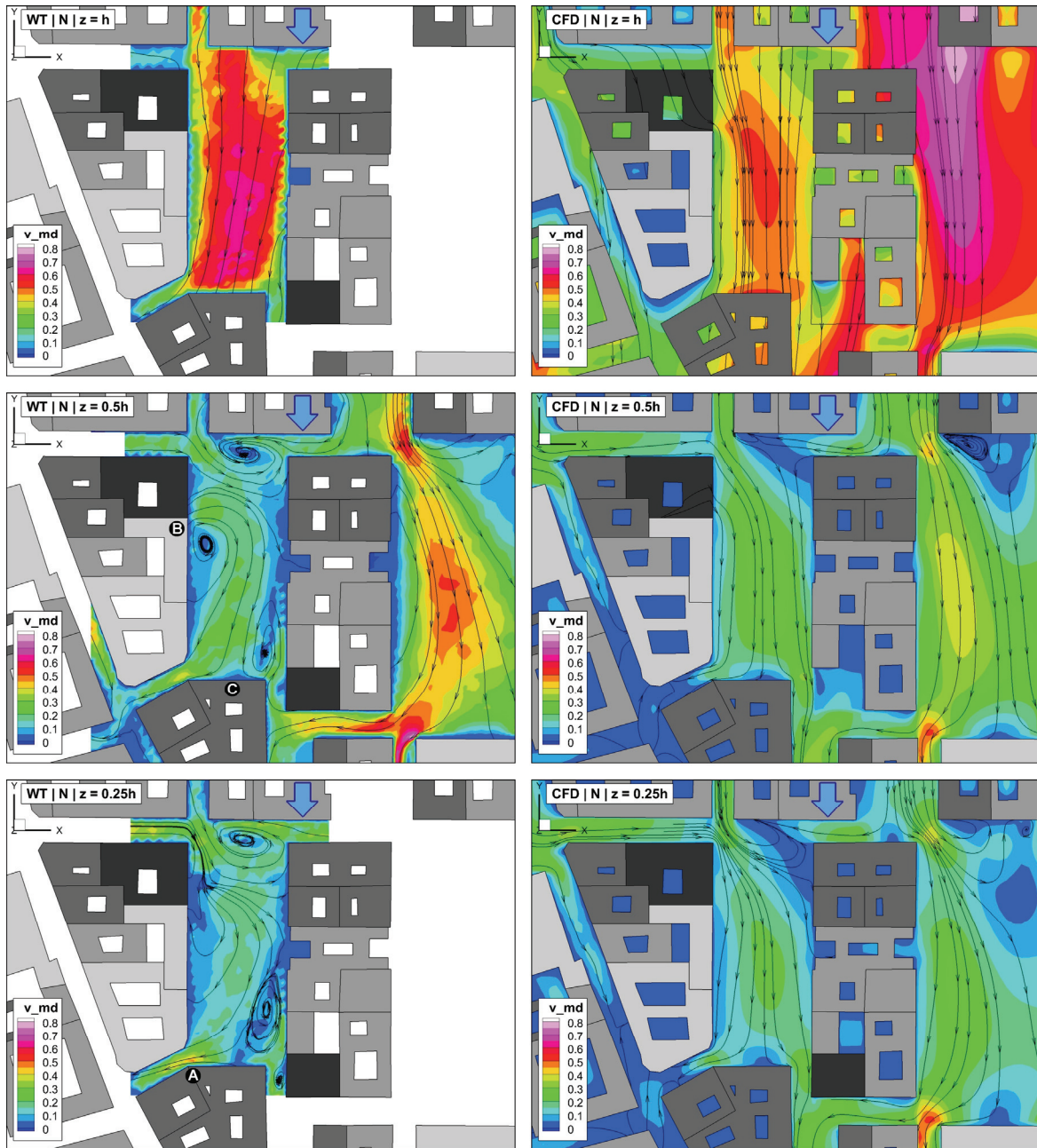

Fig. 10. Normalized horizontal velocity magnitude v_{md} distributions on three horizontal planes at northern wind direction. Left column: wind tunnel measurement; right column: CFD simulation.
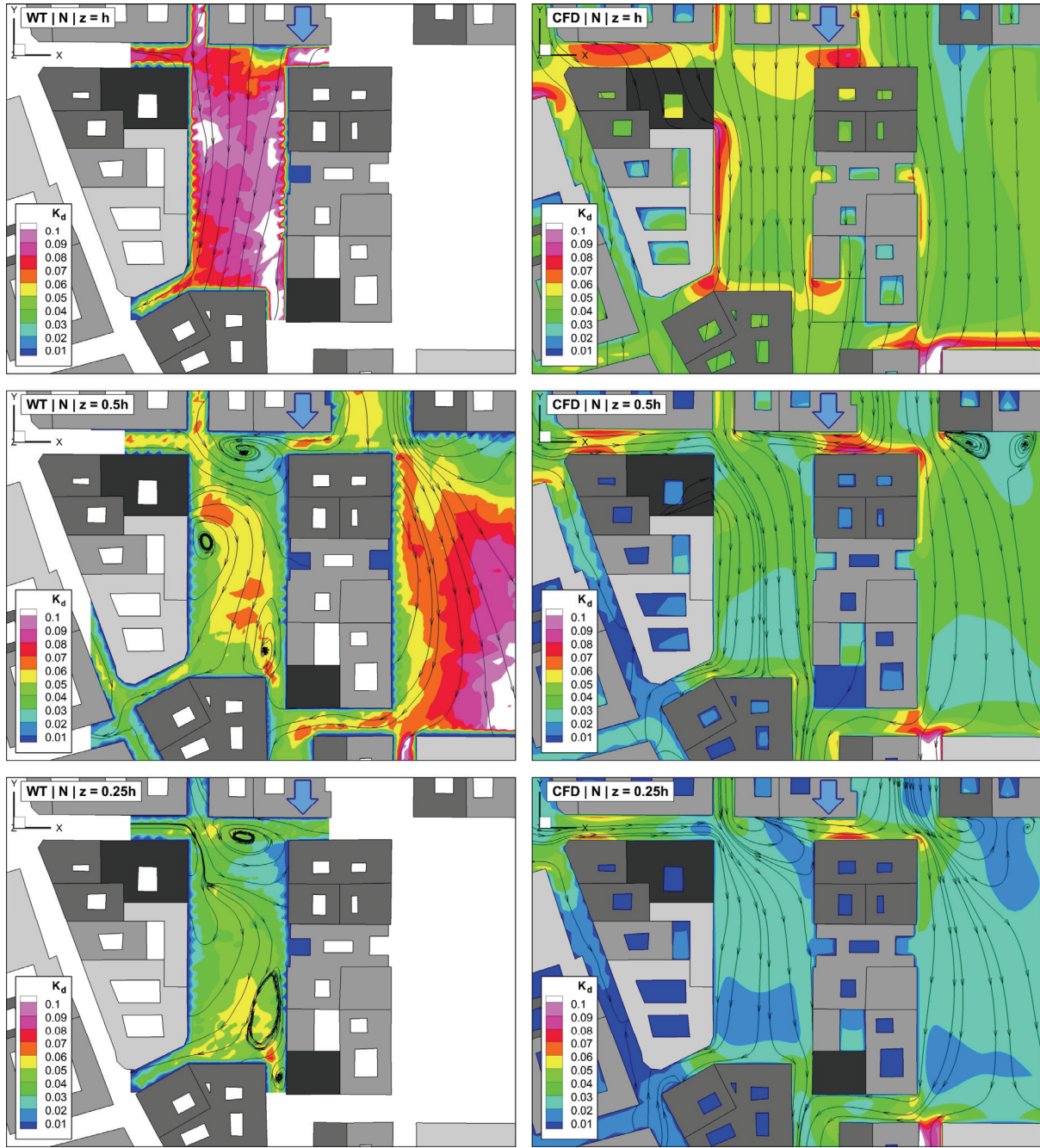
Fig. 11. Normalized turbulent kinetic energy K_d distributions on three horizontal planes at northern wind direction. Left column: wind tunnel measurement; right column: CFD simulation.

As regards the velocity fields in northern wind direction, the highest velocity values were measured at $z = h$. No backflow is observable at this height. At lower heights, mean velocity values are also lower, at 0.25 h less than 5–25% of the reference wind speed in the square itself. Top wind speed in the square is at the corner of the downstream (southern) building block, marked with A in *Fig. 10*. Outside the square, velocity magnitude of up to 0.8 can be seen at corners southward the open space in the eastern part of the measurement area.
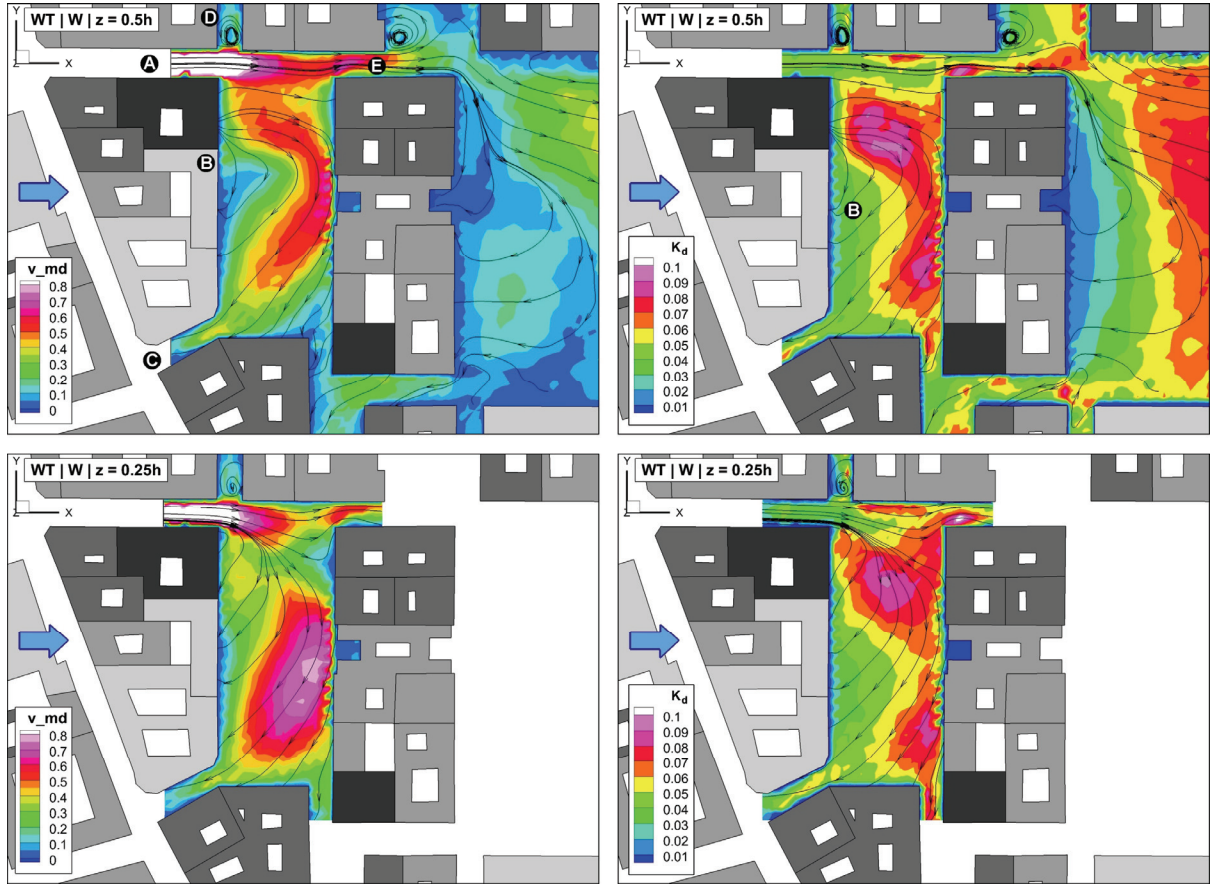
Fig. 12. Normalized horizontal velocity magnitude v_{md} (left column) and normalized turbulent kinetic energy K_d (right column) on two horizontal planes at western wind direction.

Analyzing the streamlines, it can be stated that the flow forms three major vortices in this wind direction. Their vertical extension does not reach the reference height h but is clearly present at $z = 0.25\ h$ and $z = 0.5\ h$. The northern vortex is in the separation zone of the northern block, and the middle one is obviously caused by the second, taller building of the western building block, marked with B in *Fig. 10*.

Air enters the square from the northern streets and leaves it by passing through the south-western connecting street. Interestingly, backflow is detected in the south-eastern connecting street, so the outflow is blocked here. A stagnation point can be found in the front of the southern building (marked with C in *Fig. 10*), where vertical profile VP7 suggests the presence of a horizontal vortex (B in *Fig. 7*). A significant proportion of the air, which arrives from northern connecting streets, is trapped in the first (north-eastern) vortex of the square.

CFD simulations only resolve the vortex in the north-eastern corner of the square, although in smaller size, and only visibly at 0.25 h height. While the

other vortices are suppressed, which gives a velocity field much more in line with the incident wind direction, the magnitude of velocity is about the same as in the measurement.

The average level of turbulent kinetic energy K_d (*Fig. 11*) is the simulated about 2/3 of that measured in the wind tunnel. It increases with the height and has a maximum at the average building height h. Values of the turbulent kinetic energy are usually smaller in the vicinity of the walls. This agrees well with the expectations, because both the mean velocity and the standard deviation values are lower near the walls.

Due to the stagnation point anomaly (*Kato* and *Launder,* 1993), CFD results for K_d predict peaks near building leading edges, which are not present in the measurement.

In western wind direction, flow velocities were measured along two horizontal planes at 0.25 h and 0.5 h corresponding to 7 and 14 m in full scale (20 and 40 mm in model scale). Plane 1 covers just the square and connecting streets; plane 2 covers the whole area. The velocity and turbulent kinetic energy distributions on the two horizontal planes can be seen in *Fig. 12*.

In terms of the velocity fields on the horizontal planes, it can be stated that the measured velocity values at 0.5 h are not significantly larger than the values at 0.25 h. Moreover, in the middle and eastern part of the square velocity values at 0.25 h are larger than the values at 0.5 h. The highest velocities were measured in the connecting street at the NW corner of the square at both heights; mean velocity values approximate the reference wind speed in the western part of the investigated section of the street, indicated by A in *Fig. 12*. The streamlines show that:

- The street marked by D is blocked entirely by a corner vortex.

- Most of the air passes through the square flowing from the street marked by A towards the street marked by E in *Fig. 12*.

- A smaller portion of it enters the separation bubble which is formed behind the western building block (marked by B in *Fig. 12*). However, this is modified by the high velocity inflow at the NW corner to a helical vortex, which moves air towards the southern part of the square, and pushes air through the southern connecting streets even opposite to the incident wind direction. The high velocity inflow is caused by the direct, unobstructed inflow from the river Danube (mark D in *Fig. 5*).

Thus, despite the wind coming from the west, there is a significant north to south convection in the square. It is remarkable that the flow field is very similar to that in a street canyon at slanted wind direction (*Czáder et al.,* 2009) with a huge street canyon vortex superposed to a velocity component along the street canyon.

4.3. Three-dimensionality of the flow

Because of the vertical arrangement of the LDV probe under floor, we were not able to measure the vertical velocity component w directly. However, the measured mean horizontal flow field ($\underline{v}_{hor\,d}$) let us calculate the vertical velocity gradient based on the continuity equation:

$$-\frac{\partial w_d}{\partial z} = \left(\frac{\partial u_d}{\partial x} + \frac{\partial v_d}{\partial y}\right) = div(\underline{v}_{hor\,d}). \tag{5}$$

On the horizontal ground surface, obviously w must be 0. At a small height, slightly above the ground surface, vertical velocity, if there is any, must decrease towards the surface. Thus, we can distinguish three cases for the w velocity component in horizontal planes near the ground:

a. the flow is horizontal ($w = 0$), thus $\partial w/\partial z = 0$ and $div(v_{hor\,d}) = 0$,

b. vertical inflow occurs ($w < 0$), flow towards the ground must be decelerated ($\partial w/\partial z < 0$), thus the flow field in horizontal plane will diverge ($div(v_{hor\,d}) > 0$),

c. vertical outflow occurs ($w > 0$), flow accelerates upwards ($\partial w/\partial z > 0$), and the horizontal flow field will converge ($div(v_{hor\,d}) < 0$).

In conclusion, positive values of the horizontal divergence near the ground are related to updrafts, while negative values indicate downdrafts. The relationship is demonstrated at 0.25 h height in plot a and b of *Fig. 13* using CFD results at northern wind direction. Divergence calculated from wind tunnel data in northern and western wind direction is shown in plot c and d of *Fig. 13*. The results are obviously subject of considerable noise; however, the major spots of vertical air movements are clearly recognizable.

- In case of northern wind direction, *updrafts in the wake* of the northern (upstream) building block and at building walls of the north-eastern corner can be seen, as well as a downdraft in the northern centre of the square caused by the inflow at the northeast corner.

- In case of western wind direction, the magnitude of divergence is significantly larger and shows a *single, massive helical vortex* with horizontal axis dominating the square, causing updrafts on the western and downdrafts on the eastern side.

- Up- and downdrafts can be seen in many of the connecting streets in both wind directions. Considering the direction of streamlines in the streets, these indicate *weak helical vortices* (street canyon vortices with some advection along the street axis).
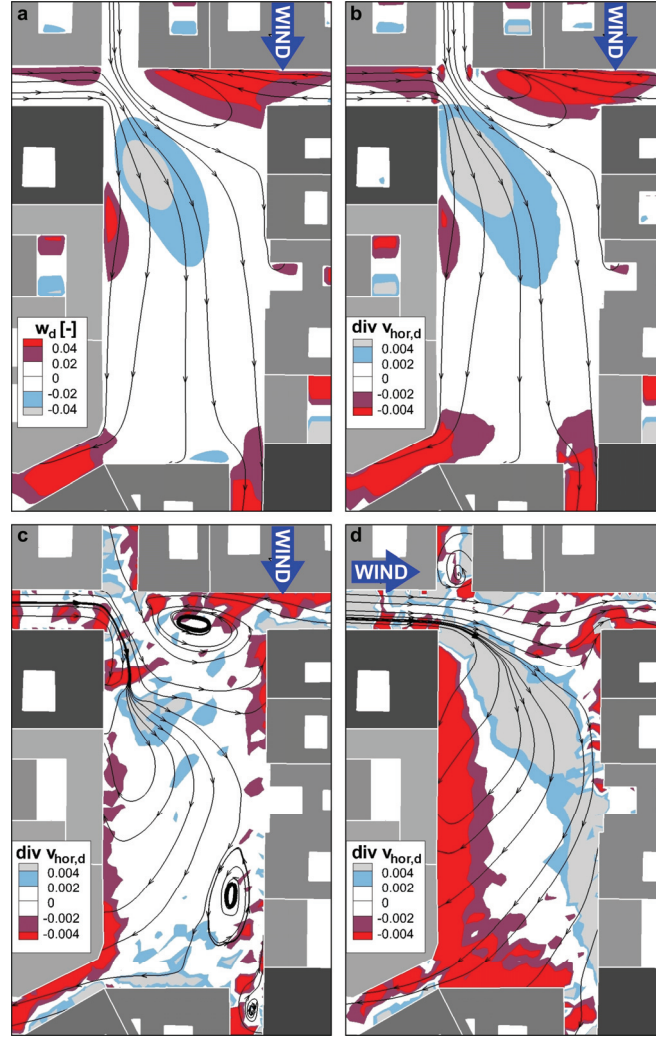
Fig. 13. Vertical air velocity and horizontal divergence in the square at 0.25 h height. Reddish colors: updraft, light colors: downdrafts. Values close to 0 are blanked. From left to right: (a) CFD simulation: normalized vertical velocity in northern wind direction; (b) CFD simulation: $\text{div}(v_{hor\ d})$ in northern wind direction; (c) wind tunnel measurement: $\text{div}(v_{hor\ d})$ in northern wind direction, (d) wind tunnel measurement: $\text{div}(v_{hor\ d})$ in western wind direction.

4.4. Analysis wind speed and direction fluctuations

The time-resolved LDV data captured simultaneously for both horizontal wind directions contain information about turbulence anisotropy and spectral properties. Up to this point, from the turbulent quantities, only turbulent kinetic energy was analyzed.

For a more detailed analysis, simultaneous u and v time series were captured at a horizontal plane at $0.5\,h$ height at several measurement locations, and the occurrence frequency of the instantaneous horizontal wind vector $\underline{v}_{i,d}$ at a certain location was visualized by wind roses (polar area diagrams). Thirty one selected wind roses are shown in *Fig. 14*, colored by

the instantaneous velocity magnitude. Also, streamlines colored by the average horizontal velocity magnitude v_{md} are shown.

- Each illustrated wind rose is placed at the location of the given measurement point.

- The roses are divided into 10-degree spokes representing the probability of 10-degree wind direction sectors.

- Each spoke is subdivided into color-coded bands that show velocity ranges.

Fig. 14. Flow field and wind roses in the investigated area in northern wind direction at 0.5 *h* height. Streamlines are colored by normalized average velocity magnitude v_{md}, buildings by their full scale height, and wind roses by the magnitude of the instantaneous normalized wind vectors $\underline{v}_{i,d}$. Note that the two velocity scales are different. The wind roses show the occurrence frequency of 10-deg wind direction sectors.

It is important to point out that as opposed to the usual application of wind roses – representing annual wind statistics –, the current wind roses show the statistics of wind speed and direction at a single incident wind direction. The wind roses presented in *Fig. 14* can be organized into different groups based on their shape:

1. Wind roses with a single dominant wind direction and small deviations can be found in streets with one-directional flow (WR2, 24) channeled along the streets' main axis. Backflow (90–270 degree to the main wind direction) is negligible. While the average velocity magnitude is 0.3–0.4, wind velocities of larger than 1 (wind gusts) have also a significant probability.

2. Fan-tail shaped wind roses appear in several locations on the square, but not in the connecting streets (WR 7, 8, 10, 12, 14–16, 19, 20, 31). Obviously, far from walls which restrict perpendicular movements, velocities can fluctuate in all directions. Deviations of up to +/–90 degree from the main wind direction can occur; also, a low percentage of backflow can be seen.

3. Wind roses with more than one peak can be observed in streets (WR 3, 21, 26, 27). The double peaks mean that at a given wind direction, flow is coming once from one end of the street, once from the other end. WR 26, located in an intersection, shows peaks 90 degree to each other, which can be explained by the angle of the connecting streets.

4. Wind roses with more than one peak can be seen also near the core of vortices of the mean wind field (WR 5, 11, 21). This can be explained by the slight movement of the vortex core, meaning that the measurement location is once on one side, and once on the other side of the vortex core, thus flow direction is reversed.

5. Finally, points on the boundary of a vortex of the mean flow can have multiple peaks, again explained by the slight movement of the cores as in WR 30. Here, instantaneous velocity magnitude reaches 0.6, while average velocity is just 0.05.

Regarding the temporal sequence of velocity fluctuations, double peaks in the histogram of velocity time series recorded in location types 4 and 5 prove the periodic switching between wind directions. *Fig. 15* shows the continuous velocity histograms of the v_d stream-wise velocity component, as captured by the LDV system. The wind rose WR 15, classified as type 2 shows a more Gaussian-like distribution; in contrast to this, the type 5 wind rose WR 30 shows double peaks indicating periodic or mode-locking flow switching between a northern (positive v_d) and a southern (negative v_d) flow state. The consequences of such flow switching on pollutant dispersion are significant, see, e.g., the

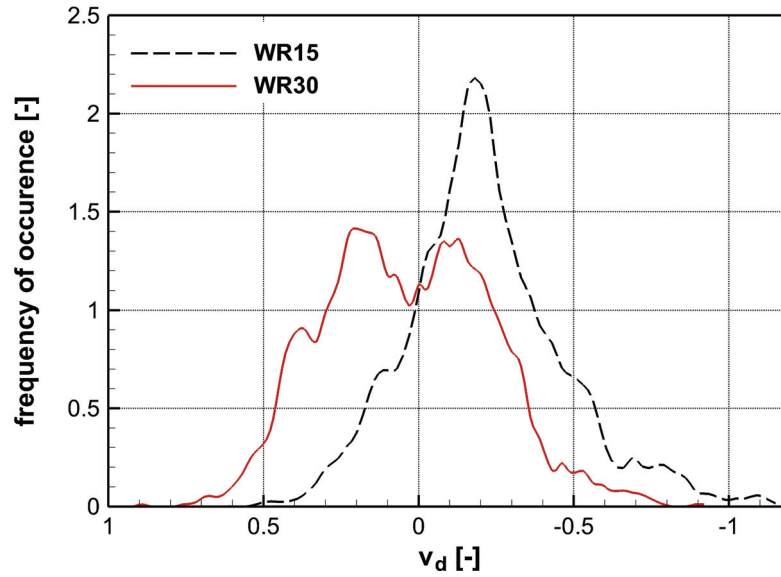observations of *Klein et al.* (2011) made at smoke plume dispersion visualisations in urban environment.

Fig. 15. Comparison of type 2 (WR 15) and type 5 (WR 30) wind velocity distributions (northern wind direction).

4.5. *CFD results and their validation with the experimental data*

The secondary objective of this paper is to show the applicability of a CFD RANS model, predominantly used in the regulatory and consulting field, in a complex urban environment. The model was able to resolve some, but not all of the flow structures dominating the square in question. The surface flow direction in the streets connected to the square is well predicted in four from five cases (see *Fig. 10*). Velocity magnitudes are qualitatively well predicted. More problems were experienced with turbulence: the prediction of K_d is often wrong, and does not give the model any information on the anisotropic and occasionally mode switching behavior of the flow discovered in Section 4.4, which has obvious consequences for dispersion phenomena, too.

In *Table 1,* hit rates of the CFD simulation are summarized. Hit rate q is defined as the percentage of those simulation data (prediction) which are inside an allowed range of the measurement (observation):

$$ q = \frac{N}{n} = \frac{1}{n}\sum_{i=1}^{n} N_i \quad with \quad N_i = \begin{cases} 1 \; for \; \left|\frac{P_i - O_i}{O_i}\right| \le D \; or \; |P_i - O_i| \le W \\ 0 \; else \end{cases}, \tag{7} $$

where P_i are the prediction (simulation) data, O_i are the observation (measurement) data, D is the allowed relative deviation, e.g. 25%, W – allowed absolute deviation or threshold, usually the measurement uncertainty of the observation.

Table 1. Hit rates calculated for the MISKAM simulations. Note that the velocity component parallel to the approach flow is *v* in northern wind and *u* in western wind direction

	Number of points	**Hit rate [%] for variable:**			
		u_d	v_d	v_{md}	K_d
Allowed relative dev. D [-]		0.25			
Allowed absolute dev. W [-]		0.026	0.026	0.03	0.006
Vertical profiles	601	36	76	74	9
Horizontal planes	1855	28	29	33	32

Hit rate calculations were performed for all vertical profiles and all horizontal planes separately, all together for 2456 measurement points, and for different variables. As it could be seen earlier in Section 4.1, vertical profiles of streamwise flow velocity above rooftop level agreed the best with the measurement (*Figs. 7 and 8*). Thus, their hit rates are accordingly high. Flow in horizontal planes is much more difficult to predict, and hit rates are generally lower on horizontal planes. Lateral flow velocity and turbulent kinetic energy were less well predicted than the streamwise velocity, and have consequently worse hit rates.

It must be noted that hit rates for calculations made by the same model, but for different test cases, might be significantly different: hit rate is also a measure for the difficulty of the test case, and not only for the performance of the model.

4.6. Comparison with fully built-up area

In the following, the CFD model is applied to answer questions regarding different urban planning scenarios. As mentioned already in the introduction, creating new urban squares by removal of defunct building blocks is often part of urban redevelopment programmes. The question is what the consequences of such a transformation on the ventilation of the whole area are. To create a reference case representing the situation before such a transformation, a numerical model was set up, in which the square was replaced by a building block consisting of four buildings of various height (23, 32, 26, and 29 m) as shown in *Fig. 16b*. CFD simulation results obtained with this geometry of a fully built-up area can then be compared with the ones with the existing square that represents the situation after the hypothetical redevelopment. Comparison is limited to the prevailing northern wind direction.
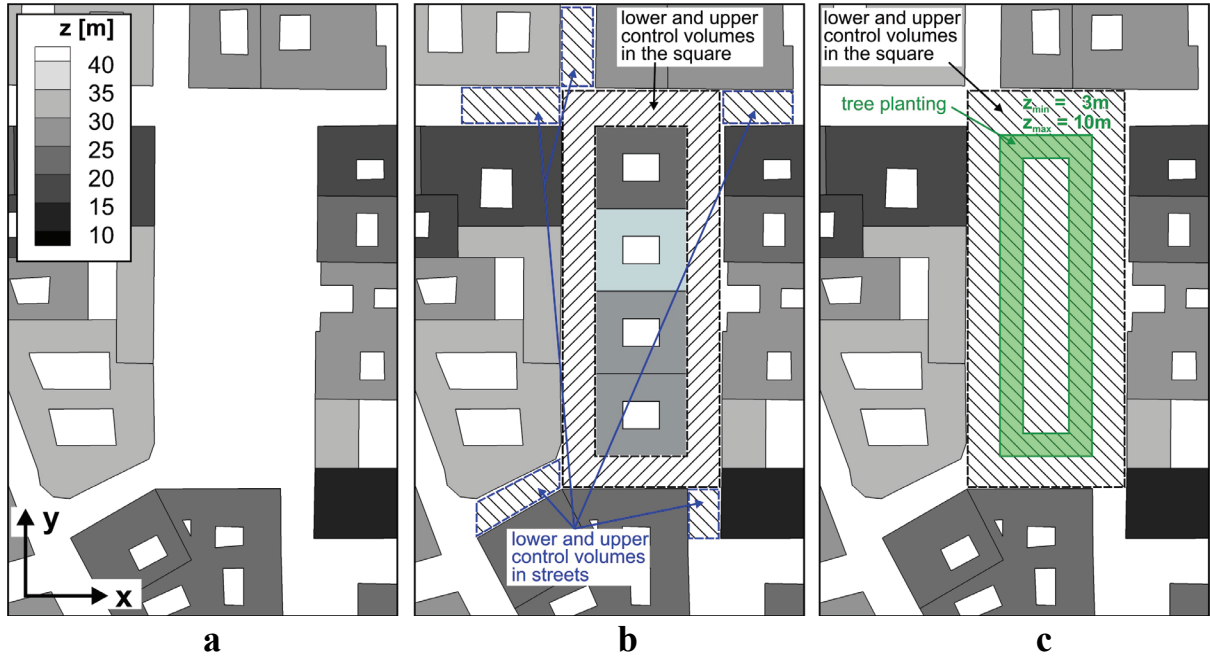
Fig. 16. (a) actual geometry of the square, (b) built-up area instead of the square representing a reference case *before* a hypothetical urban redevelopment programme; right: square with tree planting. Hatched areas with dashed borders show the control volumes used for averaging.

To perform a statistical analysis of the simulation results obtained, v_{md} and K_d are averaged for the control volume depicted in *Fig 16b* (hatched areas). The control volume consists of four parts: lower volumes from 0 to 0.5 *h* and upper volumes from 0.5 *h* to *h* height on the square itself and in the connecting streets, respectively.

In *Table 2,* the averaged variables are shown for the two cases and then the percent change $\Delta v_{md}[\%] = [v_{md}$ *(with square)* - v_{md} *(built-up area)]* / v_{md} *(built-up area)* is listed. Percent change of turbulent kinetic energy ΔK_d [%] is similarly defined.

The data in *Table 2* suggest that average wind speed on the square itself is overall increasing, but only by 2% when establishing a square compared with a fully built-in area. Such slight change consists of a significant increase of v_{md} above 0.5 *h* and a decrease of less extent below it. The average wind speed in the connecting streets increases dramatically upon removal of the central building block. At low level, below 0.5 *h*, the change is more than 50%. The comparison of turbulence from CFD results is in light of the discrepancies observed previously and is not fully to be trusted, nevertheless K_d in connecting streets is increasing, and on the square itself decreasing.

Table 2. Changes of average velocity magnitude and turbulent kinetic energy in the square and in connecting streets when comparing a built-up area and area with square. Δv_{md} [%]= [v_{md} (with square) − v_{md} (built-up area)] / v_{md} (built-up area), ΔK_d [%] similarly defined

	v_{md} built-up area	v_{md} area with square	Δv_{md} [%]	K_d built-up area	area with square	ΔK_d [%]
in the square						
below 0.5h	0.164	0.138	**−16%**	0.049	0.032	−35%
above 0.5h	0.251	0.285	**14%**	0.084	0.063	−25%
average from 0 to h	0.207	0.211	**2%**	0.066	0.047	−29%
in connecting streets						
below 0.5h	0.108	0.166	**54%**	0.036	0.047	30%
above 0.5h	0.145	0.184	**27%**	0.065	0.076	17%
average from 0 to h	0.126	0.175	**39%**	0.051	0.062	21%

4.7. Influence of vegetation

The increase of urban vegetation is seen undoubtedly as a positive measure to improve sustainability and human comfort in today's urban architecture. As in an urban square the flow is much less obstructed by buildings than in street canyons, thus we expect a remarkable influence of vegetation on flow velocities.

In the simplified model investigated in wind tunnel, the influence of vegetation has been neglected, although a proper method to model vegetation in wind tunnel tests has already been developed by *Gromke* (2011).

The CFD model MISKAM allows the modeling of vegetation using a porosity approach, as described by *Eichhorn* (2011) and validated by wind tunnel experiments by *Balczó et al.* (2009) and *Czáder et al.* (2009). The vegetation defined as a porous medium exerts an influence on the fluid flow by its viscous and form drag (*Gross,* 1993). The total drag force, e.g., in *x* coordinate direction, is described by the following formula:

$$F_{veg,x} = \rho\, c_{d0}\, bu |\underline{v}| \, , \tag{6}$$

where ρ is the fluid density [kg/m^3]; c_{d0} is the leaf drag coefficient [-]; b is the leaf area density (LAD), the projected leaf surface area per unit volume [m^2/m^3]. The obtained drag force is embedded in the RANS equation as a negative

source. Furthermore, the effects of vegetation on the turbulence are also taken into account by extending the $K\text{-}\varepsilon$ equations with new terms.

The tree planting's shape at the square (*Fig. 16*, right) is simplified: we study a homogeneous tree crown region of rectangular shape from 3 m to 10 m height and 8 m width. The centre of the region is empty, imitating a usual urban park with grass area in the middle. Leaf area density (LAD) throughout the crown region is assumed 1 m^2/m^3 based on the data of *Larcher* (2001), which is a typical value for urban tree plantings.

Table 3 summarizes the obtained results with tree planting and the comparison with the treeless case. Similarly to Section 4.6, v_{md} and K_d are averaged for two control volumes below and above 0.5 h. However, in this case the whole square is covered by the control volume (hatched area in *Fig. 16*, right). Decrease of velocity magnitude v_{md} by 21% below 0.5 h can be observed. Above 0.5 h the influence is negligible. The same can be said as regards turbulent kinetic energy, the value in the square is decreased by 27% below 0.5 h height. The change of K_d is also detectable above 0.5 h (–5%).

Table 3. Influence of tree plantings as determined by CFD simulations

	v_{md} without trees	v_{md} with trees	Δv_{md} [%]	K_d without trees	with trees	ΔK [%]
below 0.5 h	0.138	0.108	–21%	0.032	0.023	–27%
above 0.5 h	0.285	0.281	–1%	0.063	0.059	–5%
average from 0 to h	0.211	0.195	–8%	0.047	0.041	–13%

Looking at flow field plots of the CFD simulation with tree planting (not shown here), some further observations could be made: velocity decreases up to 30% inside the tree crowns. In some locations outside the crown region, the flow accelerated slightly, due to displacement effect of the trees. K_d is decreasing not only in the control volume, but also in the connecting streets, up to 30 m distance from the square. These preliminary findings fit well the observations made by *Gromke* and *Ruck* (2009) and *Balczó et al.* (2009) about the influence of vegetation in a street canyon, although a more detailed analysis might reveal further details.

5. Conclusions

The urban square investigated, although slightly simplified in geometry, can be seen as a test case of high complexity level, similarly to real urban areas. Despite this fact, the results allow more generalized conclusions to be made, which can be valid for squares of similar size:

- Average pedestrian level wind speed on the square, while significantly smaller than the above rooftop wind speed, is varying with wind direction strongly between normalized values of 0.1 and 0.5. Wind gusts can be higher than the average wind speed at rooftop level on a few locations.

- The exact location of high-speed spots in the square near the ground depends on wind direction, but is usually near building corners and at the mouth of connecting streets.

- The square influences flow in the connecting streets as well. Flow is induced in these by the developing flow structures in the square even in perpendicular or opposite direction to the approach wind. CFD results suggest that wind speed can increase up to 50% in the connecting street compared to a case in which no square is present.

- In both investigated wind directions, distinct and complex flow fields were observed, as a result of superposition of flow advection, corner vortices, separation bubbles, street canyon, and horseshoe vortices. These average flow fields are supposed to have major influence on wind comfort of pedestrians and the dispersion of pollutants, the latter of which is an objective of future studies on the square.

- For the study of flow unsteadiness, the representation of two-dimensional time-resolved data in the form of wind roses (polar area diagrams) placed over the average flow field proved to be a useful tool. Wind roses could be classified according to their shape to identify the spots, where turbulence is non-isotropic and/or flow direction is alternating.

- Tree plantings in the square are decreasing wind velocity and turbulence in the square affecting mainly the lower half of the square, where the tree crowns are located. However, turbulence changes have further reaching influence in the upper half of the square and in connecting streets, too.

We applied the MISKAM microscale flow model to the case geometry. The estimation of the measured flow field is reasonable, when average velocity magnitude comes into question. Despite the large difference in the incoming turbulence, K_d is only underpredicted by about one third on average.

However, there are certain non-negligible flaws of the simulation, like smaller or fully suppressed vortices in the mean flow field on the square. These errors can

be traced back to the commonly known turbulent kinetic energy overprediction of K-ε type closures in stagnation points.

The flow intermittency effects not resolved by MISKAM are originated from the steady RANS approach used by this class of models. As, e.g., *Letzel et al.* (2008), *Nakayama et al.* (2014) have shown, large eddy simulation (LES) applied in an urban environment can give superior results in this regard, although at the cost of much higher computational time and power requirements, which are mostly unavailable at the moment among the users of CFD models in the regulatory / urban planning field.

Recommendations for urban planning

The implications of our observations on urban planning are manifold. The flow structures in an urban square result from incoming and outgoing flow through the connecting streets. As observed, even a single gap in a building block or a lower building can modify the flow field significantly in the square. Thus, measures of local governments like permission to raise buildings to uniform height around the square will influence the flow field in the vicinity.

When establishing a new urban square in a fully built-up area, an overall increase of wind speed in neighboring streets can be expected, which will increase ventilation of the area. While this is an advantage, the high speed spots observed near the corners of connecting streets in the square might be less welcome and can cause human discomfort. However, as vegetation can decrease wind speeds locally, planting of trees on proper locations can help avoiding too high local wind speeds.

An urban (re)development project, such as establishing a new square, or the building or replacement of buildings in an urban neighborhood can be optimized using CFD tools like the MISKAM model used in this paper. One can find the optimal building configuration or the best tree planting patterns, hence the outcome of such a project can be improved in respect of quality of living.

LIST OF SYMBOLS

Name	unit	definition
b	m^2/m^3	leaf area density (LAD): projected leaf surface area per unit volume
c_{d0}	-	leaf drag coefficient
d_0	m	displacement height
$F_{veg,x}$	N/m^3	drag force from vegetation in x coordinate direction
h	m	average building height
I_u , I_v, I_w	-	turbulence intensity in x, y, and z direction
K	m^2/s^2	turbulent kinetic energy
K_d	-	dimensionless turbulent kinetic energy
$L_{u,x}$	m	integral length scale of turbulence in x direction
q	%	hit rate
u, v, w	m/s	velocity components in x, y, and z direction
$\bar{u}$, $\bar{v}$, $\bar{w}$	m/s	averaged velocity components in x, y, and z direction
u_{ref}	m/s	reference wind speed
u_d, v_d, w_d	-	dimensionless wind velocity x, y, and z direction
$\underline{v}$	m/s	flow velocity vector
$\underline{v}_{hor\,d}$	-	dimensionless velocity vector in horizontal (xy) plane
v_{md}	-	dimensionless velocity magnitude in horizontal direction
z_{ref}	m	reference height (height of the modelled boundary layer)
Δv_{md}	-	difference of dimensionless velocity magnitude between two cases
Δv_{md} [%]	-	percent difference of dimensionless velocity magnitude between two cases
ρ	kg/m^3	fluid density
σ_u, σ_v, σ_w	m/s	standard deviation of velocity in x, y, and z direction
σ_{ud}, σ_{vd}, σ_{wd}	-	dimensionless standard deviation of velocity in x, y, and z direction

References

Ahmad, K., Khare, M., and *Chaudhry, K.,* 2005: Wind tunnel simulation studies on dispersion at urban street canyons and intersections - a review. *J. Wind Engin. Indust. Aerodynam. 93*, 697–717.

Balczó, M., Balogh, M., Goricsán, I., Nagel, T., Suda, J. M., and *Lajos, T.,* 2011: Air quality around motorway tunnels in complex terrain – Computational Fluid Dynamics modeling and comparison to wind tunnel data. *Időjárás 115,* 179–204.

Balczó, M. and *Eichhorn, J.,* 2009: Refined MISKAM simulations of the Mock Urban Setting Test. Proceedings of the XXIII. MicroCAD International Scientific Conference, Miskolc, Hungary, 19–20 March 2009, 7–12.

Balczó, M., Gromke, C., and *Ruck, B.*, 2009: Numerical modeling of flow and pollutant dispersion in street canyons with tree planting. *Meteorol. Z.18,* 197–206.

Balczó, M. and *Lajos, T.,* 2012: Active reduction of air pollutant concentrations at an urban square. Proceedings of the 8th International Conference on Urban Climate (ICUC 8), Dublin, Ireland, August 6-10, 2012.

Bastigkeit, I., 2011: Erzeugung von Validierungsdaten für wirbelauflösende mikroskalige Strömungs- und Ausbreitungsmodelle. PhD thesis, University of Hamburg.

Belalcazar, L.C., Clappier, A., Blond, N., Flassak, T., and *Eichhorn, J.,* 2010: An evaluation to the estimation of road traffic emission factors from tracer studies. *Atmos. Environ. 44,* 3814–3822

Belcher, S.E., Coceal, O., Hunt, J.C.R., Carruthers, D.J., and *Robins, A.G.,* 2013: Atmospheric Dispersion Modelling Liaison Committee Report: ADMLC-R7 Annex B: A review of urban dispersion modelling

Benson, J., Ziehn, T., Dixon, N.S., and *Tomlin, A.S.,* 2007: Global sensitivity analysis of a 3D street canyon model - Part II: Application and physical insight using sensitivity analysis, *Atmos.Environ.42,* 1874–1891.

Blocken B. ,2014: 50 years of computational wind engineering: past, present and future. *Journal of Wind Engin. Indust. Aerodynam. 129,* 69–102.

Britter, R.E. and *Hanna, S.R.,* 2003: Flow and dispersion in urban areas. *Ann. Rev. Fluid Mechanics 35,* 469–496.

Czáder, K., Balczó, M., and *Eichhorn, J.,* 2009: Modelling of flow and dispersion in a street canyon with vegetation by means of numerical simulation. Proceedings of the XXIII. MicroCAD International Scientific Conference, Miskolc, Hungary, 19-20 March 2009, 47–52.

Donnelly, R.P., Lyons, T.J., and *Flassak, T.,* 2009: Evaluation of results of a numerical simulation of dispersion in an idealised urban area for emergency response modelling. *Atmos. Environ.43,* 4416–4423.

Eichhorn, J., 2011: MISKAM - Manual for version 6, Giese-Eichorn, Wackernheim, Germany

Eichhorn, J. and *Kniffka, A.,* 2010: The numerical flow model MISKAM: State of development and evaluation of the basic version. *Meteorol. Z. 19,* 81–90.

Eichhorn, J., Schrodin, R., and *Zdunkowski, W.,* 1988: Three-dimensional numerical simulations of the urban climate. *Beit. Physik Atmosphäre 61,* 187–203.

ESDU, 1972: Characteristics of wind speed in the lower layers of the atmosphere near the ground: strong winds (neutral atmosphere). Engineering Sciences Data Unit 72026

ESDU, 2001: Characteristics of atmospheric turbulence near the ground Part II: single point data for strong winds (neutral atmosphere). Engineering Sciences Data Unit 85020

Flassak, T., Janicke, U., and *Ketzel, M.,* 2010: Comparison of ground-level centreline concentrations calculated with the models OML, AERMOD/PRIME, MISKAM and AUSTAL2000 against the Thompson wind tunnel data set for simple stack-building configurations. 13th International Conference on Harmonisation within Atmospheric Dispersion Modelling for Regulatory Purposes, Paris, 1.-4. June 2010. Paper No. 163.

Franke, J., Hellsten, A., Schlünzen, H., and *Carissimo, B.,* 2007: Best practice guideline for the CFD simulation of flows in the urban environment. COST Office, Brussel

Gadilhe, A., Janvier, L., and *Barnaud, G.,* 1993: Numerical and experimental modelling of the three-dimensional turbulent wind flow through an urban square. *J. Wind Engin. Industrial Aerodynam. 46–47,* 755–763.

Goricsán, I., Balczó, M., Balogh, M., Czáder, K., Rákai, A., and *Tonkó, Cs.,* 2011: Simulation of flow in an idealised city using various CFD codes. *Int. J. Environ. Poll. 44,* 359–367.

Gromke, C. and *Ruck, B.,* 2005: Die Simulation atmosphärischer Grenzschichten in Windkanälen. Proc. 13. GALA Fachtagung: "Lasermethoden in der Strömungsmesstechnik", 6 – 8 September 2005, BTU Cottbus.

Gromke, C. and *Ruck, B.,* 2009: On the impact of trees on dispersion processes of traffic emissions in street canyons. *Bound-Lay. Meteorol. 131,* 19–34.

Gromke, C., 2011: A vegetation modeling concept for Building and Environmental Aerodynamics wind tunnel tests and its application in pollutant dispersion studies, *Environ. Pollut. 159,* 2094–2099.

Gross, G., 1993: Numerical Simulation of Canopy Flows. Springer Verlag.

Hertwig, D., Efthimiou, G.C., Bartzis, J.G., and *Leitl, B.,* 2012: CFD-RANS model validation of turbulent flow in a semi-idealized urban canopy. *J.Wind Engin. Indust. Aerodynam. 111,* 61–72.

Kato, M. and *Launder, B.,* 1993: The modelling of turbulent flow around stationary and vibrating square cylinders. Ninth Symposium on Turbulent Shear Flows, Kyoto, Japan, August 1993, 10.4.1–10.4.6.

Klein, P., Leitl, B., and *Schatzmann, M.,* 2011: Concentration fluctuations in a downtown urban area. Part II: analysis of Joint Urban 2003 wind-tunnel measurements. *Environ. Fluid Mech. 11,* 43–60.

Kozmar, H., 2011: Wind-tunnel simulations of the suburban ABL and comparison with international standards. *Wind Structures 14,* 15–34

Larcher, W., 2001: Ökophysiologie der Pflanzen. Stuttgart, Verlag Eugen Ulmer.

Letzel, M.O., Krane, M., and *Raasch, S.,* 2008: High resolution urban large-eddy simulation studies from street canyon to neighbourhood scale. *Atmos. Environ. 42,* 8770–8784.

Letzel, M.O., Flassak, T., and *Angel D.,* 2012: Verbesserung der AUSTAL2000-Ergebnisse durch Strömungs- und Turbulenzübernahme aus MISKAM. Gefahrstoffe Reinhaltung der Luft 72, Juli/August 2012, 329–333.

Leuzzi, G., Balczó, M., Amicarelli, A., Monti, P., Eichhorn, J., and *Thomson, D.J.,* 2010: Street canyon concentration estimation coupling the RANS model MISKAM and the micromixing Lagrangian model LAGFLUM. Proceedings of the 13th International Conference on Harmonization within Atmospheric Dispersion Modelling for Regulatory Purposes (HARMO13), Paris, France, June 1-4, 2010. 821–825.

Nakayama, H., Leitl, B., Harms, F., and *Nagai, H.,* 2014: Development of local-scale high-resolution atmospheric dispersion model using large-eddy simulation. Part 4: turbulent flows and plume dispersion in an actual urban area. *J. Nuclear Sci. Technol. 51,* 626–638

Olesen, H., Baklanov, A., Bartzis, J., Barmpas, F., Berkowicz, R., Brzozowski, R., Buccolieri, R., Carissimo, B., Costa, A., Di Sabatino, S., Efthimiou, G., Franke, J., Goricsán, I., Hellsten, A., Ketzel, M., Leitl, B., Nuterman, R., Polreich, E., and *Tavares, R.,* 2008: The MUST model evaluation exercise: Patterns in model performance. *Croatian Meteorolog. J. 43,* 403–408.

Olesen, H.R., Berkowicz, R.L, Ketzel, M., and *Løfstrøm, P.,* 2009: Validation of OML, AERMOD/PRIME and MISKAM using the Thompson wind tunnel data set for simple stack-building configurations. *Bound-Lay. Meteorol. 131,* 73–83.

Parra, M., Santiago, J., Martín, F., Martilli, A., and *Santamaría, J.,* 2010: A methodology to urban air quality assessment during large time periods of winter using computational fluid dynamic models. *Atmos. Environ. 44,* 2089–2097.

Rákai, A., and *Kristóf, G.,* 2013: Microscale Obstacle Resolving Air Quality model evaluation with the Michelstadt case. *The Scientific World Journal 2013,* Article ID 78174

Schatzmann, M., Olesen, H.R., and *Franke, J.,* 2010: COST 732 Model Evaluation Case Studies: Approach and Results. Brussels, COST Office.

VDI, 2004: VDI 3738 Part 12. Environmental meteorology - Physical modelling of flow and dispersion processes in the atmospheric boundary layer. Application of wind tunnels. VDI Commission for Air Quality Management, Düsseldorf.

VDI, 2005: *VDI 3783, Blatt 9: Environmental meteorology - Prognostic microscale windfield models - Evaluation for flow around buildings and obstacles.* VDI Commission for Air Quality Management, Düsseldorf.